Shap. Mem. Superelasticity
https://doi.org/10.1007/s40830-025-00580-7

ORIGINAL RESEARCH ARTICLE

Direct Comparison of Molecular Dynamics Models for Superelasticity in NiTi

Daegun You[1] · Ahmed Sameer Khan Mohammed[1] · Huseyin Sehitoglu[1]

Received: 1 July 2025 / Revised: 4 August 2025 / Accepted: 27 August 2025

Abstract Shape memory alloys (SMAs) are known for their ability to revert to their original shape upon unloading, exhibiting what is known as superelasticity behavior. Traditional continuum-based constitutive models rely heavily on a large number of tests to reproduce the superelasticity response. Recent studies on NiTi SMAs using molecular dynamics (MD) and the ab-initio approach based on density functional theory (DFT) have examined their behavior without the need for extensive experimental efforts. However, in presenting the MD-based models, previous work was limited to demonstrating only a few cases where the simulation was satisfactory. However, when a large number of scenarios are considered, the limitations become clear. In this work, several interatomic potentials in MD are utilized to study a wide range of conditions in NiTi SMAs. These scenarios include predicting transformation stress, tension–compression asymmetry, stress hysteresis, Clausius-Clapeyron curves, elastic moduli, recoverable strains, martensite crystal phase details, and temperature changes during the transformation. The work highlights the advantages and limitations of the MD potential models, providing a critical assessment. This paper honors the memory of Prof. Franco Furgiuele, University of Calabria. It was a privilege to be his friend and colleague. His sudden passing in summer 2024 was a profound loss for our community. He will be forever remembered for his cherished memories and profound insights into mechanical engineering (written by Prof. Sehitoglu).

Keywords Superelasticity · Shape memory alloy · Molecular dynamics · Phase transformation

Introduction

The nickel-titanium (NiTi) shape memory alloys (SMAs) have emerged as the most versatile and successful alloys due to their ability to revert to their original crystal structure upon unloading or upon cooling, a property of considerable scientific and engineering interest. The maximum strain upon unloading can be as high as 10%, which indicates significant recoverability and is a key measure of their functionality. Among the various tools to address their functional properties, molecular dynamics (MD) models have the potential to provide critical knowledge for engineering applications, including biomedical devices and actuators, ultimately leading to improved material performance [1–3]. These models offer a potential improvement over macroscopic models, enabling the examination of extreme stress states and temperature conditions that are costly to investigate experimentally. The original works on those MD potentials have shown the effectiveness of these models under very specific conditions [4–6], and comparisons of their performance have not been conducted under identical simulation conditions, which limits the ability to make direct comparisons between them. This study aims to address this need for direct comparisons of the MD models.

This article is an invited paper selected from presentations at the 13th European Symposium on Martensitic Transformations (ESOMAT 2024), held August 26–30, 2024, in Lecco, Italy, and has been expanded from the original presentation. The issue is dedicated in memory of Franco Furgiuele and was organized by Carmine Maletta, University of Calabria; Ausonio Tuissi, National Research Council of Italy, CNR – ICMATE; and Emanuele Sgambitterra, University of Calabria.

✉ Daegun You
daeguny2@illinois.edu

[1] Department of Mechanical Science and Engineering, University of Illinois at Urbana-Champaign, 1206 W Green St., Urbana, IL 61801, USA

Published online: 19 September 2025

The NiTi exhibits complex behaviors; one must appreciate the details of its mechanical moduli, which can be rather anisotropic, displaying orientation dependence that has implications for understanding texture effects. The phenomenon of superelasticity, where the transformation stress depends on orientation and external temperature; and the stress hysteresis, which relates to the stress difference between forward and reverse transformations during cyclic loading and unloading, are also difficult to predict. The previous studies have modeled superelasticity and stress hysteresis in NiTi [7, 8], which mostly rely on a single interatomic potential without systematic comparison. The transformation stresses and stress hysteresis have implications for understanding the fatigue behavior of these alloys [9, 10]. The internal temperature development has ramifications for elastocaloric cooling [11].

The MD models could potentially capture all mechanical behaviors without requiring a large number of tests. Recent studies especially showed that the applicability of MD models in the effects of porous, amorphous or nanocrystalline structures in NiTi [12–15]. Furthermore, the MD models should differentiate among the crystal structures of martensite, hence revealing the role of intermediate metastable states that can play a key role in the unique properties of these materials. The recoverable strains (which are orientation dependent) and the role of stress state effects (tension–compression) can be analyzed through MD simulations [16–19]. This detailed understanding is crucial for optimizing alloy performance in various applications [4–6, 20–30]. In reality, the performance of the MD models has not been thoroughly tested, and their limitations have not been evaluated. We acknowledge the contributions each of these models provides and note that such modeling efforts are a vital step toward a better understanding of NiTi shape memory alloys. This study aims to develop a high-throughput set of simulations, identify areas needing improvement, and select MD models that can effectively enhance and inform continuum models.

The purpose of this paper is to assess the capabilities of the four existing MD interatomic potentials for NiTi. These are developed by Ren-Sehitoglu (RS) [22], Zhong-Gall-Zhu(ZGZ) [6], Ko-Grabowski-Neugebauer (KGN) [4], and Tang-Wang-Li (TWL) et al. [5]. These potentials are based on Finnis–Sinclair (RS) [31], modified embedded atom method (ZGZ and KGN) [32], and deep learning potential [33] (TWL), respectively. The former three potentials (RS, ZGZ, and KGN) are widely used as baseline potentials for recent NiTi studies using MD, although these were developed a decade ago. The TWL serves a recent comparer potential in this study. The latter three potentials (ZGZ, KGN, and TWL) predict rather high transformation stress levels exceeding 1 GPa which is not in conformity with experiments. This is attributed to the limitations in interatomic potentials that overpredict the energy barriers. The data generated from these simulations provide essential information regarding the elastic moduli of NiTi in both phases, also revealing notable discrepancies between theoretical predictions and experimental results. A limitation in previous MD works is that a very narrow design space was often tested with these models, and in some instances, only a single simulation case was considered. We will conduct simulations under identical conditions to test these models.

One of the significant challenges encountered in tensile deformation simulations is that the stress levels appear to transition into compression and vice versa. This phenomenon is particularly concerning because it contradicts established experimental observations. This inconsistency raises questions and suggests a need for further investigation of its occurrence. Our objective is to illustrate such simulations over a broad range of temperatures and stress states.

To further illustrate the difference between the models, it is instructive to compare the energy levels and energy difference associated with the austenite and martensite phases. The energy differences in B2 and B19′ phases are comparable to earlier DFT simulations at 0 K (a baseline for each potential's intrinsic accuracy) of the order of 40 meV/atom. However, the energy difference between the phases is higher in most of the MD models compared to the RS model which stabilizes the martensite and also contributes to the large stress hysteresis. Finally, one must compare the simulations with experimental results. The stress hysteresis in experiments of NiTi point to levels between 50 and 200 MPa with forward transformation stress values of the order of 300–600 MPa at 300 K depending on the heat treatment and the composition. Many of the MD models demonstrated in this study fall outside these experimental values, predicting stress hysteresis exceeding 1 GPa in some cases.

It is essential to compare the models under identical simulation conditions; for instance, this study exercised all models using periodic boundary conditions rather than nanowires. We applied isenthalpic conditions across all models, allowing for temperature variations during the transformation. The results were also obtained under the same strain-rate conditions, and the simulation volume represented bulk material, not nanowires. Our goal is to harness the power of simulations to develop an extensive database that will enhance and inform continuum models effectively.

Methods

In Fig. 1, we illustrate the main simulation flows using MD. The austenitic phase (B2) of NiTi single crystal is initially constructed using the basis: Ni (0 0 0) and Ti (0.5 0.5 0.5). The number of atoms and the size of the supercell were chosen to be about 4000 and 80 Å, which are efficient and

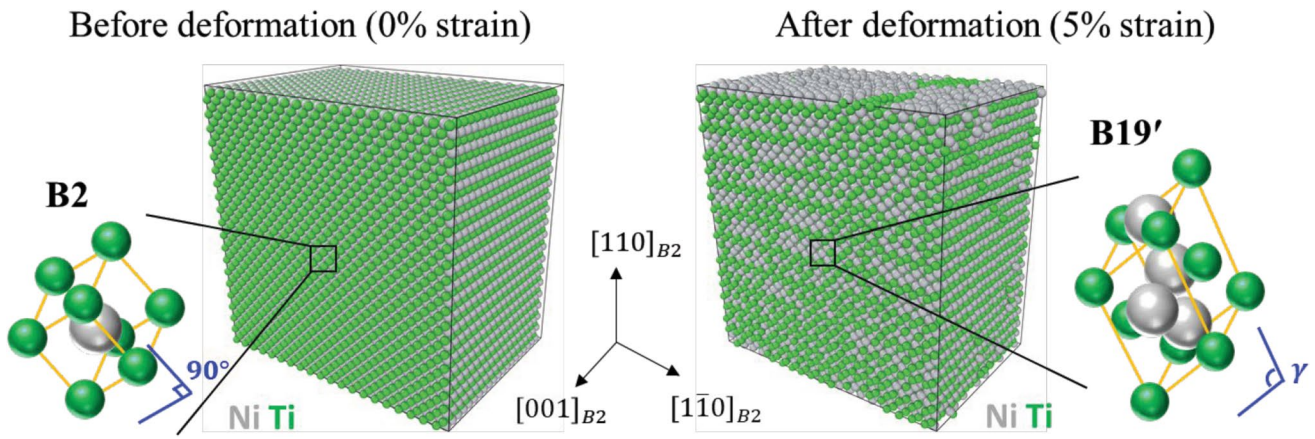

Fig. 1 Deformation-induced phase transformation in NiTi shape memory alloy (SMA): Austenite phase (B2) of single crystal before deformation (0% strain). It is transformed into the martensite phase (B19′) at 5% strain. The average structure of B19′ unit cell is usually expected as shown in the inset, which is monoclinic with one non-right angle (γ), varying from 93° to 101° depending on interatomic potentials

Table 1 Lattice parameters corresponding to the interatomic potentials [4–6, 22] used in this study, compared to the literature experiment and ab-initio calculation [34–36]

	Method/Ref	a [Å]	b [Å]	c [Å]	γ [°]
B2	MD; RS	3.021			90
	MD; ZGZ	3.008			90
	MD; KGN	2.999			90
	MD; TWL	2.999			90
	Expt.[a]	3.015			90
	DFT[b]	3.009			90
B19′	MD; RS	2.699	4.606	4.386	93.41
	MD; ZGZ	3.005	4.466	4.022	98.08
	MD; KGN	2.878	4.659	4.129	99.4
	MD; TWL	2.890	4.720	4.030	101.03
	Expt.[c]	2.898	4.646	4.108	97.78
	DFT[b]	2.929	4.686	4.048	97.8

[a]Ref. [34]

[b]Ref. [35]

[c]Ref. [36]

sufficiently large to avoid any artefacts in full periodic boundary conditions. We select a certain crystallographic orientation, such as $\langle 011 \rangle_{B2}$ and $\langle 001 \rangle_{B2}$ along loading directions for the consistency of the NiTi superelastic response [16, 17]. On the deformation, B2 phase is known to transform into a martensitic material (i.e., B19′ phase) as shown in Fig. 1. The lattice parameters of the initial B2 and B19′ phases used in this study are tabulated in Table 1 for different interatomic potentials.

Ensuring correct lattice positions is essential for identifying phases and understanding transformation mechanisms. We tabulate the lattice positions of Ni and Ti atoms in B19′ phase in Table 2 for different interatomic potentials. We recalculate the lattice positions of B19′ for KGN and TWL models by energy minimization of the primitive unit cell after random perturbation of the lattice and motif's positions. The other lattice positions are referred to the previous works [6, 22, 35, 36]. We apply up to 5 or 10% strain upon tension or compression, either along $\langle 011 \rangle_{B2}$ or $\langle 001 \rangle_{B2}$ loading direction. Upon deformation, for each interatomic potential used, the transformed phase is expected to be the B19′ phase shown in Table 2. If the transformed crystal assumes the respective Ni and Ti positions that deviate from DFT simulations or experiments, then the results for moduli, transformation strains, and stress levels are expected to differ compared to the experiments.

The present simulations were performed using the Large-scale Atomic/Molecular Massively Parallel Simulator (LAMMPS) [37]. The atomic configuration viewer Ovito [38] was used to reveal the crystal phase transformation processes. On defining the lattice positions and simulation boxes, the given structure is first energetically minimized via the conjugate gradient energy algorithm. An isenthalpic–isobaric ensemble was mainly employed for nonequilibrium deformation simulations with a constant number of atoms and zero external pressure. An isothermal-isobaric ensemble was compared when it is given. Each thermostat algorithm is utilized to maintain a steady absolute enthalpy or temperature prior to each nonequilibrium dynamics simulation. The stress–strain curves in this work are computed based on the virial stress [39]. The strain-rate in this study is set 10^{10} s^{-1}.

Superelasticity, Recoverable Strains

We focus on the stress–strain curves and discussion from different MD potentials. First, we examine the superelastic

Table 2 Atomic positions of B19′ phase of NiTi in fractional coordinates

Method/Ref.	Ti	Ni	Structure
MD; RS	0, 0, 0	0.665, 0.491, 0	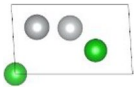
	0.341, 0.697, 0.5	0.677, 0.207, 0.5	
MD; ZGZ	0, 0, 0	0.5, 0.5, 0	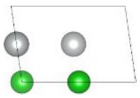
	0, 0.5, 0.5	0.5, 0, 0.5	
MD; KGN*	0, 0, 0	0.476, 0.522, 0	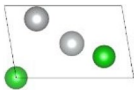
	0.295, 0.779, 0.5	0.819, 0.257, 0.5	
MD; TWL*	0, 0, 0	0.653, 0.460, 0	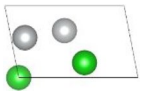
	0.209, 0.576, 0.5	0.555, 0.116, 0.5	
Expt.[a]	0, 0, 0	0.620, 0.459, 0	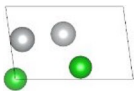
	0.165, 0.567, 0.5	0.545, 0.108, 0.5	
DFT[b]	0, 0, 0	0.630, 0.456, 0	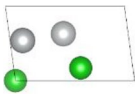
	0.171, 0.563, 0.5	0.540, 0.107, 0.5	

Lattice Ti atom is set as the origin, and the relative positions of motif Ti and Ni atoms are tabulated. Visualization of each unit cell is shown

[a]Ref. [36]

[b]Ref. [35]

*Positions are calculated in this study. See the main text

loading–unloading under tension and compression along $\langle 011 \rangle_{B2}$ direction at room temperature (RT; 300 K). To incorporate the elastocaloric mechanism, we mainly address the MD potentials within the isenthalpic-isobaric ensemble. In the following discussion, we describe the energy barriers in detail. Then we further analyze the effects of ambient or internal temperature, other orientation $\langle 001 \rangle_{B2}$, higher strain, and phase transformation based on four MD potentials.

In Fig. 2, the stress–strain curves represent the varying stiffness in the initial and deformed crystals. These are attributed to elastic moduli of B2 and B19′ in different MD potentials, as tabulated in Tables 3 and 4. For initial B2 and strained B19′ phases, elastic moduli of ZGZ, KGN, and TWL models deviate from the experiment and ab-initio results, which is reflected in the slopes of both loading–unloading regions. As the C_{44} is substantially different compared to experiments, this also affects the transformation stress and causes it to deviate from experiments. After the stress is reached at the critical value, the phase transformation from B2 to B19′ begins in various motif positions in the supercell. It includes atomistic rearrangement into a monoclinic lattice and an internal twinning process. These transformation stress levels for three MD potentials (ZGZ, KGN, and TWL) are higher than the experimental observation of about 800 MPa [17, 40], as compared to RS model.

Upon unloading, the deformed crystal (mainly B19′) undergoes the reverse transformation, followed by the lower stress levels. This implies that B19′ with internal twinning is stable under high stress and strain. Therefore, the differences in stress hysteresis of the four MD models upon unloading are ascribed to the energy required to revert the crystal to B2. To further analyze it, we characterize the energy-strain curve upon unloading in Fig. 3. KGN and TWL models represent higher energy barriers upon unloading, which is reflected in their higher stress hysteresis in Fig. 2. Their higher energy barriers are derived from the overfitted model parameters of energy values with different phases within kinetics, as tabulated in Table 5. Total energies by different MD potentials are calculated in this study. ZGZ model is based on the erroneous energy in martensite, which causes underprediction of the deformed states in finite temperatures. For KGN and TWL models, the erroneous energy levels of deformed states

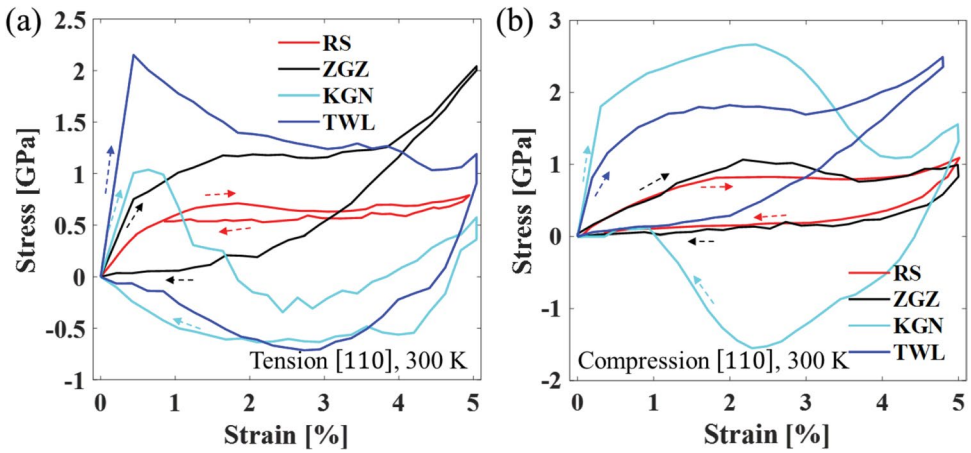

Fig. 2 Stress–strain curves for NiTi under **a** tension and **b** compression along $\langle 011 \rangle_{B2}$ orientation at room temperature (RT; 300 K) using different interatomic potentials via an isenthalpic ensemble. Loading/unloading directions are indicated by corresponding color arrows

Table 3 Elastic constants of B2 phase in NiTi (units in GPa, except the Poisson's ratio, ν, in dimensionless)

	Expt.[a]	DFT[b]	MD (This study) (RS)	MD (This study) (ZGZ)	MD (This study) (KGN)	MD (This study) (TWL)
C_{11}	162	183	146	205	156	184
C_{12}	129	146	122	136	113	176
C_{44}	35	46	35	47	74	61
B	140	158	130	159	128	178
G	28	35	26	42	53	38
E	78	98	73	116	140	106
ν	0.41	0.40	0.41	0.38	0.32	0.40

[a]Ref. [41]

[b]Ref. [42]

Table 4 Elastic constants of B19′ phase in NiTi (units in GPa, except the Poisson's ratio, ν, in dimensionless)

	DFT[a]	MD (This study) (RS)	MD (This study) (ZGZ)	MD (This study) (KGN)	MD (This study) (TWL)
C_{11}	209	206	692	178	174
C_{12}	114	72	400	77	158
C_{13}	102	103	326	61	120
C_{15}	1	2	292	− 47	14
C_{22}	234	252	1135	240	278
C_{23}	139	120	222	111	156
C_{25}	− 7	− 7	125	− 47	− 14
C_{33}	238	218	303	233	305
C_{35}	27	− 16	175	82	18
C_{44}	77	37	286	83	74
C_{46}	− 5	− 2	110	14	− 17
C_{55}	23	41	215	− 24	16
C_{66}	72	43	114	147	85
B	154	141	447	128	181
G	56	50	202	68	56
E	150	133	526	173	153
ν	0.34	0.34	0.30	0.27	0.36

[a]Ref. [19]

are attributed to its overfitting on their MD data in finite temperatures. The tension–compression asymmetry has been interpreted by different unidirectional modes that cause the other transformation direction to be unfavorable [20, 43]. Therefore, under the tension and compression, phase transformation occurs on different sets of planes and directions.

Ambient and Internal Temperature Changes

For the given loading orientation $\langle 011 \rangle_{B2}$ in Figs. 2 and 3, we investigate the temperature dependency of the NiTi superelasticity. In Figs. 4 and 5, we illustrate the stress–strain curves at higher temperatures from RT to 400 K under tension. Using the RS model, the trend agrees with the previous experiments [3]. As compared to conventional alloys, it shows increasing stress levels with increasing temperature. The martensite B19′ phase becomes unstable than austenite B2 with increasing temperature, i.e., B2–B19′ phase transformation becomes less favorable, resulting in higher stress required. With increasing temperature, the volume fraction of B19′ phase is expected to decrease, and above 450 K, the B2 phase is eventually favored in the entire crystal. Other MD potentials do not capture this trend overall, implying inaccurate prediction of phase transformation. This is discussed in a later section.

We also review the ambient temperature control and its internal changes using different MD models. In SMAs, the transformation occurs nearly under constant enthalpy during fast transformations when there is not much time for heat exchange with the surroundings. This is referred to as an isenthalpic process. In such a case, the phase transformation produces an entropy change that creates a temperature rise during transformation, and its recovery upon reverse transformation results in cooling. This is the main mechanism behind elastocaloric cooling [11, 44], commonly missed in the previous MD studies. Therefore, the isenthalpic simulations are relevant to assessing the temperature rise during superelasticity. Here, we directly compare these simulations in MD with isothermal conditions, which are commonly used in Fig. 6a. The isothermal control results in higher stress hysteresis for different MD models. This is because the circumscribed internal temperature in the isothermal condition causes the stress to rise upon loading/unloading.

In Fig. 6b, the temperature changes upon loading/unloading have been measured in the isenthalpic ensemble by different MD potentials. The temperature changes of RS and KGN models agree with the theoretical Clausius–Clapeyron prediction (~ 36 K) based on experimental specific heat [11]. Considering the stress–strain curves in Figs. 4 and 5, the KGN model's agreement with the

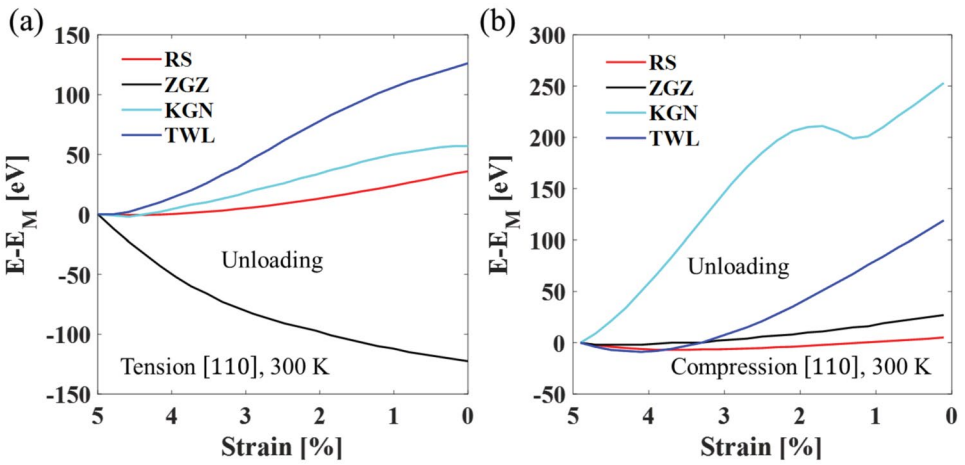

Fig. 3 Energy-strain curves upon unloading of NiTi under **a** tension and **b** compression along $\langle 011 \rangle_{B2}$ orientation at RT using different interatomic potentials via an isenthalpic ensemble. Energy changes from the martensite E_M is plotted because a strain of 5% magnitude (l.h.s of the plot) corresponds to martensitic state

Table 5 Total energies (eV/atom) of austenite, martensite, undeformed, and deformed supercells in different MD potentials

	RS	ZGZ	KGN	TWL
B2 (0 K)	− 5.079	− 5.022	− 5.049	− 6.999
B19′ (0 K)	− 5.108 (− 29)	− 5.073 (− 51)	− 5.083 (− 34)	− 7.038 (− 39)
B2 (300 K)	− 5.040 (+39)	− 4.983 (+39)	− 5.011 (+38)	− 6.943 (+56)
B19′ (300 K)	− 5.082 (− 3)	− 5.051 (− 29)	− 5.086 (− 37)	− 7.013 (− 14)
Tension $\langle 011 \rangle_{B2}$ (5%, 300 K)	− 5.037 (+42)	− 4.971 (+51)	− 4.985 (+64)	− 6.931 (+68)
Compression $\langle 011 \rangle_{B2}$ (5%, 300 K)	− 5.037 (+42)	− 4.976 (+46)	− 4.992 (+57)	− 6.929 (+70)
Unloaded 300 K	− 5.037 (+42)	− 4.975 (+47)	− 4.984 (+65)	− 6.926 (+73)

Parenthesis indicates $E - E_{B2,0K}$ in meV/atom

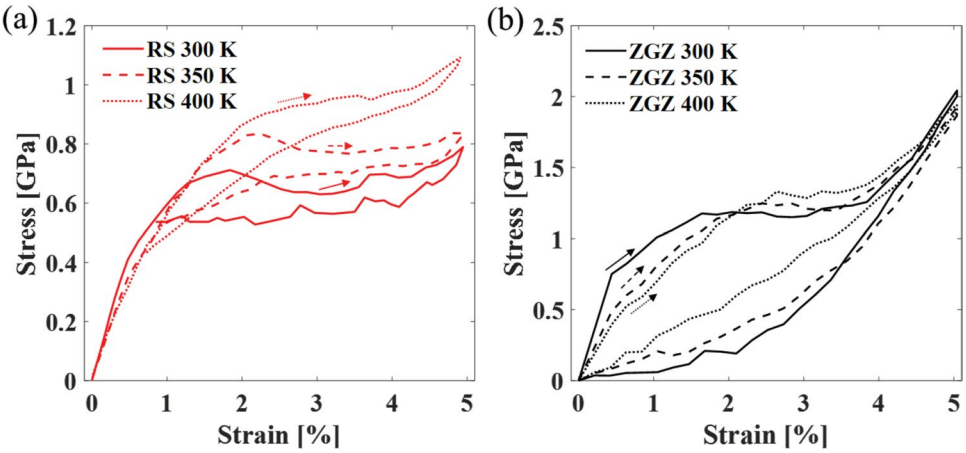

Fig. 4 Stress–strain curves for NiTi under tension along $\langle 011 \rangle_{B2}$ orientation at different ambient temperatures using **a** RS and **b** ZGZ models via an isenthalpic ensemble. Loading directions are indicated by the corresponding color and dashed arrows

theoretical prediction is ascribed to the lower stress level at the deformed crystal. The TWL model deviates from this prediction and also cannot produce the temperature recovery upon unloading. This implies an inaccurate prediction of reverse transformation. Three interatomic potentials (ZGZ, KGN, and TWL) commonly model that the crystal volume can change for nanopillar and nanowire cases [4–6, 26], where the surface energy becomes a major parameter, although the crystal volume remains the same. We note that the temperature change serves as the basis for the elastocaloric effect, which could have important practical applications on a bulk scale. The release of heat upon deformation is promoted upon martensite formation and produces thermo-mechanical coupling that needs to be reflected in continuum descriptions. This study lays the groundwork for developing the fundamental results and shows how to conduct the MD simulations to address this effect.

Orientation and Strain Effects

Here, we study the stress–strain result in other orientation such as $\langle 001 \rangle_{B2}$ different from Figs. 2, 3, 4, 5, and 6 using four MD potentials. In Fig. 7, the variation of stiffness in initial and deformed crystals is also shown, similar to $\langle 011 \rangle_{B2}$ loading orientation. The order of stiffness in the initial crystals in tension follows the elastic moduli tabulated in Table 3. However, this order is flipped in compression, the stress of RS model becomes stiffest among the models. This flip was observed in the experiment along $\langle 001 \rangle_{B2}$ loading orientation [16], as compared to $\langle 011 \rangle_{B2}$ case which has similar stiffness in tension and compression for austenite phase. Among four

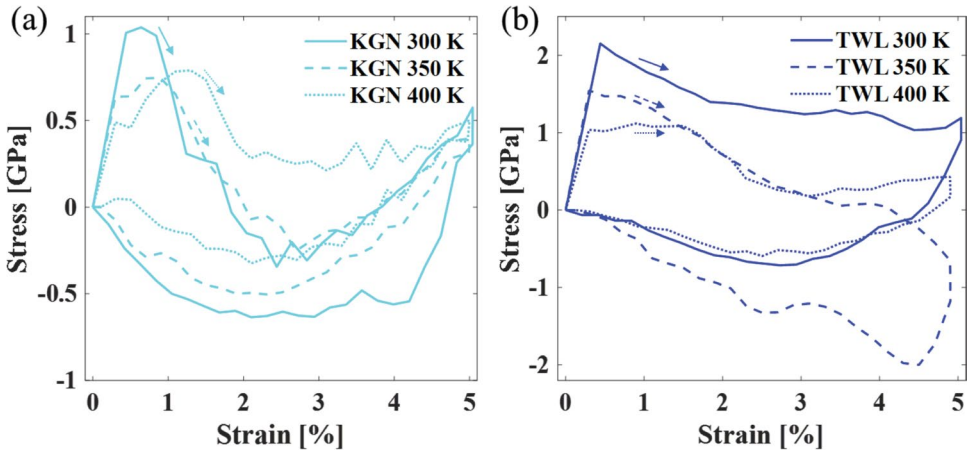

Fig. 5 Stress–strain curves for NiTi under tension along $\langle 011 \rangle_{B2}$ orientation at different ambient temperatures using **a** KGN and **b** TWL models via an isenthalpic ensemble. Loading directions are indicated by the corresponding color and dashed arrows

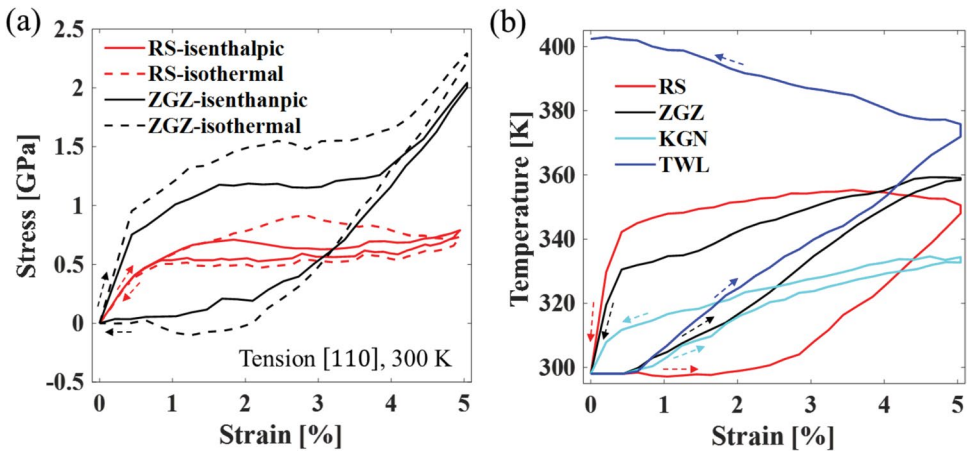

Fig. 6 **a** Stress–strain curves for NiTi under tension along $\langle 011 \rangle_{B2}$ orientation at RT within different ensembles using RS and ZGZ models. **b** Temperature (internal)-strain curves under tension along $\langle 011 \rangle_{B2}$ orientation at RT using different interatomic potentials via an isenthalpic ensemble. Loading/unloading directions are indicated by the corresponding color and dashed arrows

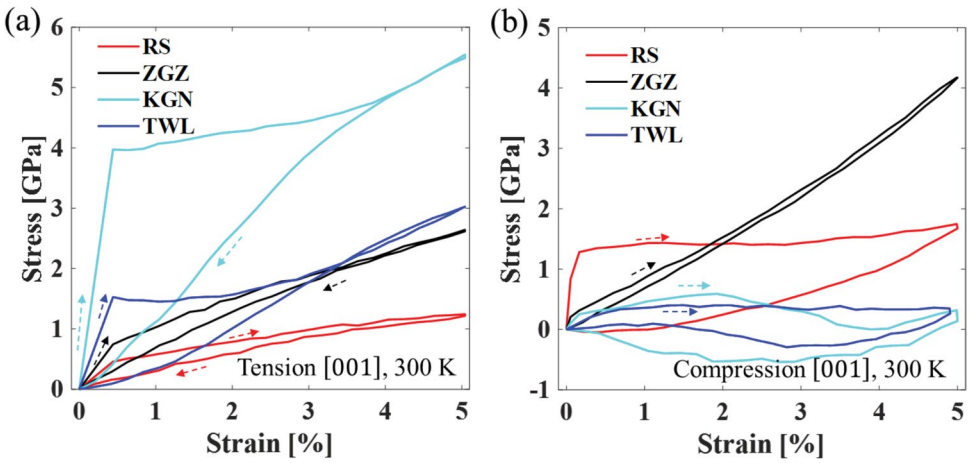

Fig. 7 Stress–strain curves for NiTi under **a** tension and **b** compression along $\langle 001 \rangle_{B2}$ orientation at RT with different interatomic potentials. Loading/unloading directions are indicated by the corresponding color and dashed arrows

MD potentials, RS model shows the stress closer to the experimental findings [16, 17] (~ 800 MPa). Other models severely deviate from it due to their inaccurate model parameter settings, such as auxiliary surface energy, as discussed in the previous section.

Along $\langle 001 \rangle_{B2}$ loading orientation at RT, further increase of strain can affect the stress levels and their hysteresis. In Fig. 8, we apply a higher strain (up to 10%) for all MD potentials in both tension and compression. Overall, the higher strain increases the stress level compared to 5% strain, which was observed in experiments [17]. About 3.5 GPa is expected up to 10% strain based on the available experimental compression, given 1.8 GPa at 7% strain. RS and TWL models closely capture this stress level at 10% strain, although TWL model underpredicts the stress at lower strain. Also, the recoverable strain in the experiment was shown to be constant after 5% strain, and the MD models closely capture this trend, except Zhong model. In $\langle 001 \rangle_{B2}$ loading orientation at RT, ZGZ model does not show any recoverable strain in both strain cases. This is mostly due to its erroneous atomic positions of B19′ phase as tabulated in Table 2. For ZGZ model, the lattice and motif's positions are assumed to be the same as B2 phase in fractional coordinates, resulting in unambiguity for phase transformation. This also reduces the accuracy of phase identification as discussed in the next section.

Phase Identification

In this section, we analyze the phase identification in deformed NiTi. Common neighbor analysis (CNA) [45, 46] is normally used in the previous MD studies [4, 15], although it is not suitable to distinguish martensite and austenite due to thermal perturbation and low symmetry in B19′ phase [47]. Instead, polyhedral template matching (PTM) [48] has been recently shown to reliably distinguish B19′ from B2 using deviation from the symmetry [49, 50]. This deviation is defined by root-mean-square-deviation (RMSD) from the basic templates such as BCC, HCP, and FCC. The cutoff RMSD of B19′ phase is usually set to 0.13 in the previous studies, and this number is based on HCP template according to the structural origin [47]. Also, the atomic positions of four different MD potentials are varying, and therefore the cutoff RMSD is different for each model. We tabulate the cutoff RMSD for each MD model in Table 6 as compared to the experiment and DFT based atomic positions.

In Figs. 2, 3, 4, 5, 6, 7, and 8, we demonstrate different orientations and strains in tension and compression. In each simulation, the initial B2 lattice evolves into monoclinic B19′ via intermediate phases, notably the R-phase [51]. The intermediate phases can persist within the deformed crystal, and defining their RMSD values is essential for an accurate phase identification. However, lattice parameters and atomic positions for the intermediate phases are not available from any of the MD potentials. Therefore, we compute the cutoff

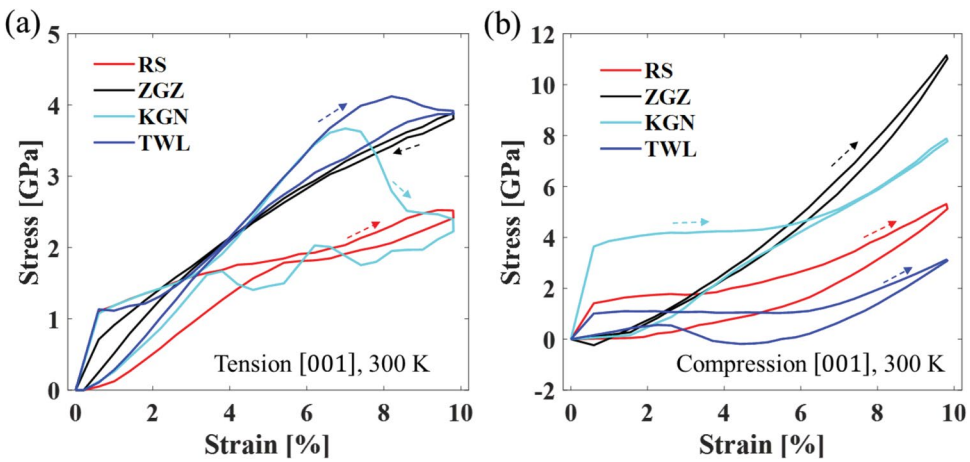

Fig. 8 Stress–strain curves for NiTi under **a** tension and **b** compression with higher strain (10%) along $\langle 001 \rangle_{B2}$ orientation at RT with different interatomic potentials. Loading/unloading directions are indicated by the corresponding color and dashed arrows

Table 6 Cutoff root-mean-square-deviation (RMSD) parameter of B19′ in polyhedral template matching (PTM) for each MD potential, experiment, and DFT

Ref	RS	ZGZ	KGN	TWL	Expt	DFT
Cutoff RMSD	0.1	0.08	0.09	0.144	0.120	0.126

Lattice parameter and atomic position of each case are based on Tables 1 and 2

RMSD propensity for each intermediate or B19′ phase using the DFT based lattice parameters and atomic coordinates, as presented in Table 7. We also include the orthorhombic B19 phase (hypothetical candidate) in the phase identification. The lattice parameters and atomic positions of DFT based B19 and R-phases are referred to Materials Project [52]. The ones of B2 and B19′ phases are based on Tables 1and 2.

Figure 9 provides a visual phase identification map of the crystal compressed to 5% strain at RT along $\langle 011 \rangle_{B2}$ orientation. Since the appropriate cutoff RMSD differs for each phase—B2, B19, R, and B19′—and the B19′ threshold varies between MD potentials, we adopt phase-specific cutoff RMSD values of 0, 0.06, 0.07, and 0.08, respectively. Both RS and KGN potentials successfully capture the full martensitic transformation in this case. In the case of ZGZ potential, as noted in the previous section, the erroneous atomic positions obscure the distinction between B19′ phase and other intermediates, thereby compromising the fidelity of phase identification. Conversely, the TWL potential produces atomic positions that closely align with DFT or experimental data; yet, its over-weighting of auxiliary parameters in the model—such as surface energy—undermines its capacity to predict the complete martensitic transformation. This implies that, under the TWL model, achieving full martensite formation in this simulation case would necessitate higher strains.

Table 7 Cutoff RMSD parameter of each phase in PTM based on the lattice parameters and atomic positions in DFT

Phase	B2	B19	R	B19′
Cutoff RMSD	0 (BCC)	0.089	0.099	0.126

In Table 8, we summarize the phase identification results for all simulations. Experimentally, a full martensitic transformation is expected in the deformed crystals for all cases. Overall, RS model most faithfully reproduces this full martensitic transformation, and the TWL potential follows. In contrast, the ZGZ and KGN potentials inaccurately capture the phase transformation depending on the case. As discussed above, these shortcomings stem from the erroneous atomic positions in ZGZ model or the over-weighting of auxiliary parameters—such as energy levels—in the TWL and KGN models, as discussed in Table 5. These results highlight the importance of selecting an appropriate MD potential for accurate SMA modeling.

Discussion of Results

Isenthalpic Condition and Heating During Transformation

As discussed in the "Ambient and Internal Temperature Changes" Sect., the MD simulations in this study were conducted primarily under isenthalpic conditions to ensure that the elastocaloric mechanism is captured. The temperature variation within the crystal resulting from entropy change (ΔS) can be estimated by using the Clausius–Clapeyron relation,

$$-\Delta S = \frac{d\sigma}{dT}\epsilon_0 = -\frac{\Delta H}{T_0} \tag{1}$$

where $\frac{d\sigma}{dT}$ is the Clausius–Clapeyron slope, ϵ_0 denotes the transformation strain, ΔH is the enthalpy change per unit volume during transformation, and T_0 represents the thermodynamic equilibrium temperature between the two phases. The slope $\frac{d\sigma}{dT}$ quantifies how the critical stress required to

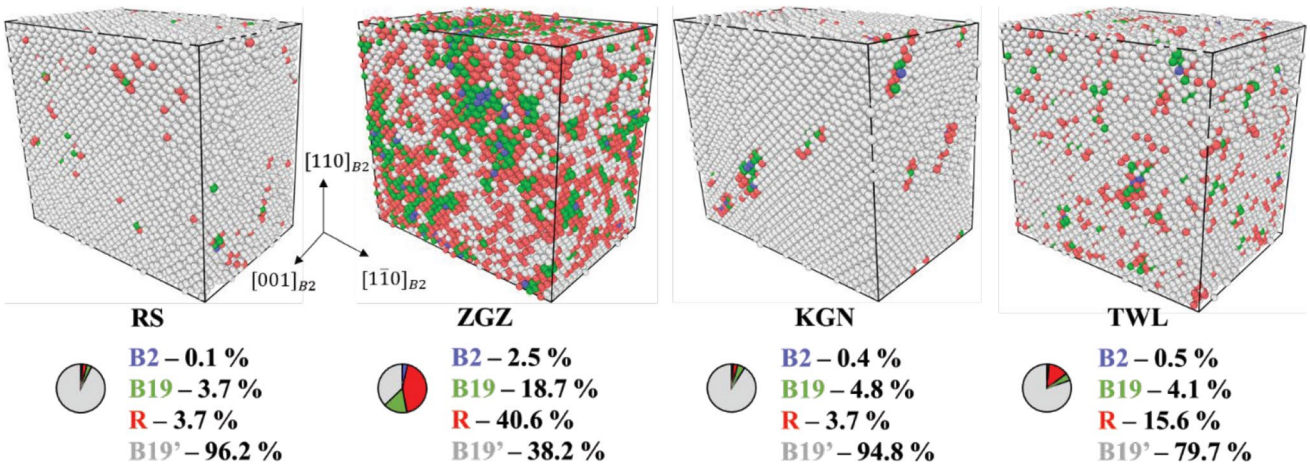

Fig. 9 Phase identifications in 5% strained NiTi under compression at RT along $\langle 011 \rangle_{B2}$ orientation in four different interatomic potentials. Polyhedral template matching (PTM) is used to identify each crystal phase (B2, B19, R, and B19′) in different colors (blue, green, red, and gray)

Table 8 Phase identification of NiTi using different interatomic potentials. Root-mean-square-deviation (RMSD) parameters (0.06, 0.07, 0.08) in PTM are used to classify B19, R, and B19′ phases, respectively. Intensity of each cell's shading reflects the prominence of the corresponding phase color (blue, green, red, and gray)

Model	RS				ZGZ				KGN				TWL			
Phase	B2	B19	R	B19′	B2	B19	R	B19′	B2	B19	R	B19′	B2	B19	R	B19′
T ⟨011⟩ – RT, 5 %	0.3 %	2.2 %	7.0 %	90.5 %	0.4 %	4.8 %	22.9 %	71.9 %	3.0 %	15.4 %	32.7 %	48.9 %	0.1 %	1.0 %	5.7 %	93.1 %
C ⟨011⟩ – RT, 5 %	0.1 %	0.8 %	2.9 %	96.2 %	2.5 %	18.7 %	40.6 %	38.2 %	0.4 %	1.4 %	3.4 %	94.8 %	0.5 %	4.1 %	15.6 %	79.7 %
T ⟨001⟩ – RT, 5 %	1.4 %	8.2 %	22.7 %	67.7 %	0.9 %	11.8 %	36.3 %	50.9 %	2.4 %	13.7 %	31.3 %	52.5 %	0.4 %	3.4 %	13.1 %	83.1 %
C ⟨001⟩ – RT, 5 %	0.2 %	1.7 %	6.8 %	91.3 %	4.4 %	30.8 %	44.5 %	20.4 %	0.7 %	5.9 %	21.5 %	71.9 %	1.0 %	6.7 %	20.4 %	71.9 %
T ⟨001⟩ – RT, 10 %	0.3 %	0.6 %	3.0 %	96.1 %	0.0 %	1.0 %	7.4 %	91.6 %	4.3 %	14.5 %	27.9 %	53.3 %	0.8 %	4.7 %	13.9 %	80.6 %
C ⟨001⟩ – RT, 10 %	0.1 %	1.5 %	5.4 %	93.0 %	0.1 %	2.0 %	14.7 %	83.3 %	1.2 %	5.7 %	19.5 %	73.5 %	0.1 %	1.0 %	5.5 %	93.4 %

induce the martensitic transformation under 0.1% tensile strain for the given orientation and temperature. To estimate the theoretical maximum adiabatic elastocaloric temperature change, ΔT_{th}, the following expression was applied,

$$\Delta T_{th} = -\frac{T}{C_p}\Delta S \tag{2}$$

where T denotes the ambient temperature such as 300 K, and C_p corresponds to the specific heat (590 J/kgK for NiTi). Experimental measurements of the parameters such as $\frac{d\sigma}{dT}$ and ε_0 are reported in the previous work [11], thereby resulting in ΔS about − 70 J/kgK for NiTi. The theoretical temperature change ΔT_{th} becomes ~ 36 K. While RS and KGN models have temperature changes closer to this prediction, all the potentials still markedly exceed the experimentally observed ΔT (~ 14 K), indicating that the entropy change inherent to the martensitic transformation is overemphasized in these models—i.e., $\frac{d\sigma}{dT}$ or ε_0 is overestimated. To better capture the true elastocaloric response using the current MD potentials, the measurement of temperature changes under the extra stress state conditions is recommended.

Twin Formation

In both tension and compression for all the MD potentials, the martensitic internal twinning plays a central role in the reversible transformation. Upon reaching the transformation stress, emerging B19′ martensite regions undergo a "compound-type" twinning on the {001} family of planes. As strain increases beyond this point, additional deformation twins develop on the same {001} systems, yielding a dense twinned microstructure by ~ 4% total strain. The formation of multiple twinned variants limits the net transformation strain: whereas single-variant growth (i.e., detwinning) can enhance recoverable strain, the coexistence of many twin variants reduces the overall martensitic distortion, and thus slightly lowers the simulated transformation strain relative to the experiment.

During unloading, the twinned martensite first elastically recovers, then detwins as the reverse B19′ to B2 transformation proceeds. The removal of applied stress destabilizes the {001} compound twin and promotes reversion to the austenite. Since the deformation twinning is unidirectional—i.e., it favors a single shear sense on specific planes—the active twin variants (and hence the critical stresses and hysteresis) differ between compression and tension. The opposite transformation direction is unfavorable, so distinct twin systems operate under each loading or unloading mode, giving rise to the observed asymmetries in different MD potentials.

Transformation Stress Magnitudes and Stress Hysteresis

Many factors govern the transformation stress magnitudes of shape memory alloys including crystal orientation, stress state, chemistry, and precipitation. The stress magnitudes for near equiatomic NiTi in tension and compression are of the order of 500–700 MPa and 700–900 MPa. The results in polycrystalline materials are close to ⟨111⟩ single crystals

as pointed by Sehitoglu et al. sometime ago [53–56]. An independent experiment also had shown 200–700 MPa in tension of polycrystalline by Sedmák et al. [57]. The presence of precipitates can modify these magnitudes as pointed by Sehitoglu et al. So, a Taylor type correction for crystal plasticity is not necessary. Some of the MD potentials in this study satisfy the transformation stress magnitudes in the specific orientations, but the stress hysteresis should be in the range of 200–400 MPa. The given MD models (e.g., RS) conform to these magnitudes but others (e.g., KGN) do not, especially entering the compressive stress regimes during the tensile straining path is contrary to experiments.

Phase Identification

A comprehensive methodology was developed to identify the crystal phases. Special codes were written to differentiate between B19′, R-phase, B19 and B2. Large volumes were sampled, showing that at strain levels of 5%, some models indicate the presence of phases other than B19′, which is unrealistic. For example, as shown in Table 8, the ZGZ model exhibits the highest occurence of intermediate phases (B19 and R) in both orientations, followed by the KGN, TWL models. The RS model provides superior predictions. The less accurate models require larger applied strains to achieve complete martensitic transformation (B19′). The ZGZ potential, for instance, greatly increases martensitic phase detection from 20.4 to 83.3% at 5% and 10% compressive strain, respectively. But, in compression of NiTi the transformation should be nearly complete near 5% strain. Both the KGN and TWL models also struggle to provide reliable phase identification as strain increases in some cases. Conversely, the RS potential consistently produces near-complete martensitic transformation across many loading scenarios. The poor performance of the ZGZ, KGN, and TWL models stems from their initial parameterization under specific conditions like nanowires, which overemphasize surface energy effects. Consequently, these potentials are biased toward nanoscale behavior, resulting in inaccurate phase transformation and stress level predictions in bulk NiTi.

Additionally, the RMSDs of rhombohedral R-phase and hypothetical B19 are below the B19′, as the next larger local lattice distortions away from the austenite. Thus, those regions, which have only partially transformed along the pathway B2 → R → B19′, fall into the R-phase bin, while the other regions with further insufficient strain are prematurely classified as hypothetical B19 phase. This reflects the two-step transformation sequence: early-stage produces R-phase distortions (RMSD: 0.099), whereas completion of the next step converts R into B19′ with a relatively smaller RMSD increment (RMSD: 0.099 → 0.126). The fact that the additional RMSD from R to B19′ is smaller than that from B2 to R is consistent with the idea that the R → B19′ involves an lattice-invariant shear (LIS) operation, as discussed in the previous work [51]. The R-phase can be internally twinned (such as {110} and {100} compound twins) with a higher number of habit plane variants within LIS than the single-step B2 → B19′ transformation. In this aspect, some of MD models suggest that incomplete progression through the B2 → R step leads to coexisting local configurations that are crystallographically closer to R than to either the B2 or the fully transformed B19′. These factors should be considered when selecting or developing interatomic potentials for engineering applications involving NiTi or other shape memory alloys.

Energy Changes During Transformation

During the austenite–martensite transformation in NiTi alloy, the internal energy of control volume evolves with the corresponding stress level. As tabulated in Table 5, the martensite at RT has lower energy than the austenite for all the MD models ($E_M - E_{B2}$; RS: − 42 meV/atom; ZGZ, KGN, TWL: ~ − 70 meV/atom). Then the deformation-induced austenite–martensite transformation is pronounced unless the elastocaloric effect is large. In the meanwhile, the deformation-induced twinning in the martensite also raises the energy of system, introducing a barrier that should be overcome. This is similar for unloading such as the detwinning and reverse martensite-austenite transformation. The magnitude of this combined energy change (transformation and twinning/detwinning) directly determines the requisite stress variation, and therefore provides a sensitive measure of interatomic potential accuracy. For instance, some of the MD models (such as ZGZ, TWL) examined in this study produce markedly higher energy changes ($E - E_M$; ZGZ: ~ − 120 eV, TWL: ~ 125 eV) rather than the RS model (~ 35 eV) as shown in Fig. 3a. It consequently leads to a deviation of stress levels in their stress–strain responses, implying inaccurate hyper-parameters of these models. The RS model shows the smallest energy change in both tensile and compressive loadings (Fig. 3b), which lead the stress levels in agreement with the experiment.

Elastic Moduli

The topic of elastic moduli has been widely misunderstood since early research on the stress–strain response of NiTi alloys [19]. The elastic moduli of austenite and martensite differ based on atomistic calculations, with martensite moduli being higher. However, in experiments, the moduli measurements, especially for martensite, do not always reflect the fully detwinned state, depending on the unloading point during the cycle. The martensite moduli change depending on whether the martensite is twinned or a single crystal.

Previously, the multi-variant structure showed lower values compared to single-crystal moduli. All the MD models examined in this study demonstrate the nonlinear evolution of martensite, as evidenced by the unloading curves. The difficulty is that the absolute values of martensite moduli are off (much higher than experiments with ZGZ, KGN, and TWL potentials, except the RS model) in a number of these MD models as discussed earlier. The main issue with the use of high moduli is threefold: (1) Accurate constitutive response of SMAs as applied to stents [58] and other biomedical applications, constitutive models as reviewed in textbooks [59] and review articles [60] and for prediction of fatigue response [9], (2) when displacements are measured with digital image correlation, such as near crack tips, and the stress intensity is determined, a modulus value needs to be used. For the far field, the austenite moduli need to be correct while for the near-field martensite values have to be accurate. This issue was explained in a number of papers on NiTi [61] and other shape memory alloys [62]; (3) the deformation in the martensitic state is followed by heating to achieve constrained recovery in several applications involving civil engineering problems with spring confinement of concrete [63] or in mechanical engineering where coupling is achieved with rings [64]. The correct martensite modulus is needed to simulate the response correctly.

Linking to Continuum

A number of semi-empirical continuum models, some with thermo-mechanical coupling and finite element method (FEM) implementation, have been developed [65–69]. There is also a large class of micro-mechanical models that treat the transformation similarly to crystal plasticity with modifications to predict volume fraction evolution and tension–compression asymmetry [70–72]. Texture effects and hardening have been accounted for upon interaction of variants in these micro-mechanical models. These continuum models have merit, but there is a clear need to develop new ones that capture the basic attributes of these alloys (such as thermos-mechanical coupling, stress hysteresis, intermediate phases) highlighted in this study.

Final Remarks

We regret omitting some of the very early MD models, which also have merit, but were excluded for the sake of brevity. We note the works of Farkas on B2 [73], the austenite phase. Lai and Liu [74, 75] model is the basis of the ZGZ model. The MD simulations have been applied to understand the role of precipitates [21] in NiTi, and the results are in agreement with experiments [76], and the observation of preferred martensite variants near the precipitate [77]. This subject is beyond the scope of this paper and is left for future studies.

Conclusions

In this article, we have evaluated the fidelity of several MD interatomic potentials for NiTi SMA modeling by comparing their stress–strain responses and phase identification accuracy. For each potential, performance was systematically assessed under tensile and compressive loading, variations in ambient and internal temperature, different crystallographic orientations, and multiple strain levels. Among the MD models considered, RS potential consistently delivered the most accurate predictions of critical stress thresholds, recoverable strain, temperature evolution, and phase transformation. In contrast, ZGZ, KGN, and TWL potentials showed reduced accuracy—primarily due to erroneous atomic configurations or the over-weighting of ancillary parameters stemming from assumptions such as non-constant volume nanowire geometries. Nonetheless, when applied to the specific situation for which those geometries are reproduced, KGN and TWL potentials can still serve as effective modeling tools. Therefore, aligning the given simulation conditions with the scenarios detailed in this review is recommended to select the most appropriate potential.

We summarized various MD models, offering a revised understanding of the lattice and macroscopic behaviors of NiTi shape memory alloys (SMAs). The paper highlights the significance of atomic simulations through Molecular Dynamics (MD) in linking discrete physics with continuum models. Due to the complex elastic constants, elastocaloric effects, tension–compression asymmetry, and evolving transition crystal states in SMAs, creating MD potentials that accurately include these details is challenging. Overcoming this challenge is crucial for advancing future modeling techniques in the field.

Acknowledgements It is with great appreciation that this paper is prepared to honor Prof. Franco Furgiuele. The work is supported by the National Science Foundation grant DMR-2125821. This support is gratefully acknowledged.

Data Availability Data will be made available on request.

References

1. Miyazaki S, Otsuka K, Wayman CM (1989) The shape memory mechanism associated with the martensitic transformation in Ti-Ni alloys—I. Self-accommodation. Acta Metall 37(7):1873–1884
2. Miyazaki S, Otsuka K, Wayman CM (1989) The shape memory mechanism associated with the martensitic transformation in Ti-Ni alloys—II. Variant coalescence and shape recovery. Acta Metall 37(7):1885–1890
3. Otsuka K, Ren X (2005) Physical metallurgy of Ti–Ni-based shape memory alloys. Prog Mater Sci 50(5):511–678
4. Ko W-S, Grabowski B, Neugebauer J (2015) Development and application of a Ni-Ti interatomic potential with high predictive accuracy of the martensitic phase transition. Phys Rev B 92(13):134107
5. Tang H, Zhang Y, Li Q-J, Xu H, Wang Y, Wang Y, Li J (2022) High accuracy neural network interatomic potential for NiTi shape memory alloy. Acta Mater 238:118217
6. Zhong Y, Gall K, Zhu T (2011) Atomistic study of nanotwins in NiTi shape memory alloys. J Appl Phys 110(3):033532
7. Zhu X, Li S, Zhou S, Song X, Dui G (2025) Synergistic effects of strain rate and temperature on the superelastic–plastic behaviors of nanocrystalline NiTi shape memory alloy: a molecular dynamic study. J Appl Phys 137(17):175101
8. Zhu X, Li S, Zhou S, Yuan H, Dui G (2025) Effects of strain rate on the superelasticity of polycrystalline NiTi shape memory alloy with microvoids: constitutive modeling and molecular dynamics. Acta Mech 236(2):1381–1394
9. Pelton AR (2011) Nitinol fatigue: a review of microstructures and mechanisms. J Mater Eng Perform 20(4):613–617
10. Sidharth R, Mohammed ASK, Sehitoglu H (2022) Functional fatigue of NiTi shape memory alloy: effect of loading frequency and source of residual strains. Shape Mem Superelasticity 8(4):394–412
11. Pataky GJ, Ertekin E, Sehitoglu H (2015) Elastocaloric cooling potential of NiTi, Ni2FeGa, and CoNiAl. Acta Mater 96:420–427
12. Ko W-S, Choi WS, Xu G, Choi P-P, Ikeda Y, Grabowski B (2021) Dissecting functional degradation in NiTi shape memory alloys containing amorphous regions via atomistic simulations. Acta Mater 202:331–349
13. Zhu X, Li S, Wang Y, Dui G (2025) Atomistic simulation of porous nanocrystalline NiTi shape memory alloy considering coupling effects of transformation and plasticity. Vacuum 240:114546
14. Zhu X, Liu C, Wang Y, Dui G (2025) Effects of pores on the superelasticity coupled with plasticity in nanocrystalline NiTi shape memory alloys: a molecular dynamic study. J Mater Res Technol 37:1324–1341
15. Ko W-S, Maisel SB, Grabowski B, Jeon JB, Neugebauer J (2017) Atomic scale processes of phase transformations in nanocrystalline NiTi shape-memory alloys. Acta Mater 123:90–101
16. Gall K, Sehitoglu H, Chumlyakov YI, Kireeva IV (1999) Tension–compression asymmetry of the stress–strain response in aged single crystal and polycrystalline NiTi. Acta Mater 47(4):1203–1217
17. Sehitoglu H, Jun J, Zhang X, Karaman I, Chumlyakov Y, Maier HJ, Gall K (2001) Shape memory and pseudoelastic behavior of 51.5%Ni–Ti single crystals in solutionized and overaged state. Acta Mater 49(17):3609–3620
18. Wang J, Sehitoglu H (2013) Twinning stress in shape memory alloys: theory and experiments. Acta Mater 61(18):6790–6801
19. Wang J, Sehitoglu H (2014) Martensite modulus dilemma in monoclinic NiTi-theory and experiments. Int J Plast 61:17–31
20. Chowdhury P, Guowu R, Sehitoglu H (2015) NiTi superelasticity via atomistic simulations. Philos Mag Lett 95(12):574–586
21. Chowdhury P, Patriarca L, Ren G, Sehitoglu H (2016) Molecular dynamics modeling of NiTi superelasticity in presence of nano-precipitates. Int J Plast 81:152–167
22. Ren G, Sehitoglu H (2016) Interatomic potential for the NiTi alloy and its application. Comput Mater Sci 123:19–25
23. Wang J, Sehitoglu H (2012) Resolving quandaries surrounding NiTi. Appl Phys Lett 101(8):081907
24. Chowdhury P, Sehitoglu H (2017) Deformation physics of shape memory alloys – fundamentals at atomistic frontier. Prog Mater Sci 88:49–88
25. Chowdhury P, Sehitoglu H (2017) A revisit to atomistic rationale for slip in shape memory alloys. Prog Mater Sci 85:1–42
26. Zhong Y, Gall K, Zhu T (2012) Atomistic characterization of pseudoelasticity and shape memory in NiTi nanopillars. Acta Mater 60(18):6301–6311
27. Mohammed ASK, Sehitoglu H (2020) Modeling the interface structure of type II twin boundary in B19' NiTi from an atomistic and topological standpoint. Acta Mater 183:93–109
28. Mohammed ASK, Sehitoglu H (2020) Martensitic twin boundary migration as a source of irreversible slip in shape memory alloys. Acta Mater 186:50–67
29. Ataollahi S, Mahtabi MJ (2024) Atomistic simulation of the effect of H-phase precipitate on the transformation temperatures and stress-induced phase transformation in Ni-rich NiTiHf. Shape Mem Superelasticity 10(2):189–197
30. Yazdandoost F, Mirzaeifar R (2018) Stress wave and phase transformation propagation at the atomistic scale in NiTi shape memory alloys subjected to shock loadings. Shape Mem Superelasticity 4(4):435–449
31. Finnis MW, Sinclair JE (1984) A simple empirical N-body potential for transition metals. Philos Mag A 50(1):45–55
32. Baskes MI (1992) Modified embedded-atom potentials for cubic materials and impurities. Phys Rev B 46(5):2727–2742
33. Wang H, Zhang L, Han J, E W (2018) DeePMD-kit: a deep learning package for many-body potential energy representation and molecular dynamics. Comput Phys Commun 228:178–184
34. Goo E, Sinclair R (1985) The B2 to R transformation in Ti50Ni47Fe3 and Ti49.5Ni50.5 alloys. Acta Metall 33(9):1717–1723
35. Huang X, Ackland GJ, Rabe KM (2003) Crystal structures and shape-memory behaviour of NiTi. Nat Mater 2(5):307–311
36. Kudoh Y, Tokonami M, Miyazaki S, Otsuka K (1985) Crystal structure of the martensite in Ti-49.2 at.%Ni alloy analyzed by the single crystal X-ray diffraction method. Acta Metall 33(11):2049–2056
37. Thompson AP, Aktulga HM, Berger R, Bolintineanu DS, Brown WM, Crozier PS, in 't Veld PJ, Kohlmeyer A, Moore SG, Nguyen TD, Shan R, Stevens MJ, Tranchida J, Trott C, Plimpton SJ (2022) LAMMPS - a flexible simulation tool for particle-based materials modeling at the atomic, meso, and continuum scales. Comput Phys Commun 271:108171
38. Stukowski A (2010) Visualization and analysis of atomistic simulation data with OVITO–the open visualization tool. Model Simul Mater Sci Eng 18(1):015012
39. E.B. Tadmor, R.E. Miller, Modeling materials: continuum, atomistic and multiscale techniques, Cambridge university press2011.
40. Orgéas L, Favier D (1998) Stress-induced martensitic transformation of a NiTi alloy in isothermal shear, tension and compression. Acta Mater 46(15):5579–5591

41. Mercier O, Melton KN, Gremaud G, Hägi J (1980) Single-crystal elastic constants of the equiatomic NiTi alloy near the martensitic transformation. J Appl Phys 51(3):1833–1834
42. Hatcher N, Kontsevoi OY, Freeman AJ (2009) Role of elastic and shear stabilities in the martensitic transformation path of NiTi. Phys Rev B 80(14):144203
43. Christian JW, Mahajan S (1995) Deformation twinning. Prog Mater Sci 39(1):1–157
44. Furgiuele F, Magarò P, Maletta C, Sgambitterra E (2020) Functional and structural fatigue of pseudoelastic NiTi: global vs local thermo-mechanical response. Shape Mem Superelast 6(2):242–255
45. Stukowski A (2012) Structure identification methods for atomistic simulations of crystalline materials. Model Simul Mater Sci Eng 20(4):045021
46. Tsuzuki H, Branicio PS, Rino JP (2007) Structural characterization of deformed crystals by analysis of common atomic neighborhood. Comput Phys Commun 177(6):518–523
47. Li B, Shen Y, An Q (2020) Structural origin of reversible martensitic transformation and reversible twinning in NiTi shape memory alloy. Acta Mater 199:240–252
48. Larsen PM, Schmidt S, Schiøtz J (2016) Robust structural identification via polyhedral template matching. Model Simul Mater Sci Eng 24(5):055007
49. Hua P, Wang B, Yu C, Han Y, Sun Q (2022) Shear-induced amorphization in nanocrystalline NiTi micropillars under large plastic deformation. Acta Mater 241:118358
50. Liu S, Ke CB, Cao S, Ma X, Zhao ZX, Li YW, Zhang XP (2022) An atomistic study of self-accommodation martensite morphologies and microstructure evolution during forward and reverse martensitic transformations in single crystal and bicrystal NiTi alloys. Comput Mater Sci 210:111455
51. Zhang X, Sehitoglu H (2004) Crystallography of the B2 → R → B19′ phase transformations in NiTi. Mater Sci Eng A 374(1):292–302
52. Jain A, Ong SP, Hautier G, Chen W, Richards WD, Dacek S, Cholia S, Gunter D, Skinner D, Ceder G, Persson KA (2013) Commentary: the materials project: a materials genome approach to accelerating materials innovation. APL Mater 1(1):011002
53. Gall K, Lim TJ, McDowell DL, Sehitoglu H, Chumlyakov YI (2000) The role of intergranular constraint on the stress-induced martensitic transformation in textured polycrystalline NiTi. Int J Plast 16(10):1189–1214
54. Gall K, Sehitoglu H (1999) The role of texture in tension–compression asymmetry in polycrystalline NiTi. Int J Plast 15(1):69–92
55. Gall K, Sehitoglu H, Anderson R, Karaman I, Chumlyakov YI, Kireeva IV (2001) On the mechanical behavior of single crystal NiTi shape memory alloys and related polycrystalline phenomenon. Mater Sci Eng A 317(1):85–92
56. Gall K, Sehitoglu H, Chumlyakov YI, Zuev YL, Karaman I (1998) The role of coherent precipitates in martensitic transformations in single crystal and polycrystalline Ti-50.8at%Ni. Scr Mater 39(6):699–705
57. Sedmák P, Pilch J, Heller L, Kopeček J, Wright J, Sedlák P, Frost M, Šittner P (2016) Grain-resolved analysis of localized deformation in nickel-titanium wire under tensile load. Science 353(6299):559–562
58. Duerig TW, Melton K, Stöckel D (2013) Engineering aspects of shape memory alloys. Butterworth-Heinemann
59. Machado LG, Lagoudas DC (2008) Thermomechanical constitutive modeling of SMAs, shape memory alloys: modeling and engineering applications. Springer, Boston, pp 121–187
60. Sehitoglu H, Anlas G, Mohammed ASK (2023) Shape memory alloys—frontier developments. In: Aliabadi MHF, Soboyejo WO (eds) Comprehensive structural integrity, 2nd edn. Elsevier, Oxford, pp 610–679
61. Sgambitterra E, Maletta C, Furgiuele F, Sehitoglu H (2018) Fatigue crack propagation in [0 1 2] NiTi single crystal alloy. Int J Fatigue 112:9–20
62. Sidharth R, Wu Y, Brenne F, Abuzaid W, Sehitoglu H (2020) Relationship between functional fatigue and structural fatigue of iron-based shape memory alloy FeMnNiAl. Shape Mem Superelasticity 6(2):256–272
63. Chen Q, Andrawes B, Sehitoglu H (2014) Thermomechanical testing of FeNiCoTi shape memory alloy for active confinement of concrete. Smart Mater Struct 23(5):055015
64. Niccoli F, Giovinco V, Garion C, Maletta C, Chiggiato P (2022) A simplified analytical model to simulate martensite reorientation and plasticity in shape memory alloy ring couplers. J Intell Mater Syst Struct 33(12):1497–1512
65. Boyd JG, Lagoudas DC (1996) A thermodynamical constitutive model for shape memory materials. Part I. The monolithic shape memory alloy. Int J Plast 12(6):805–842
66. Lagoudas DC (2008) Shape memory alloys. Science and Business Media, LLC
67. Brinson LC (1993) One-dimensional constitutive behavior of shape memory alloys: thermomechanical derivation with non-constant material functions and redefined martensite internal variable. J Intell Mater Syst Struct 4(2):229–242
68. Auricchio F, Taylor RL (1997) Shape-memory alloys: modelling and numerical simulations of the finite-strain superelastic behavior. Comput Methods Appl Mech Eng 143(1):175–194
69. Zaki W, Moumni Z (2007) A three-dimensional model of the thermomechanical behavior of shape memory alloys. J Mech Phys Solids 55(11):2455–2490
70. Gall K, Sehitoglu H (1999) The role of texture in tension-compression asymmetry in polycrystalline NiTi (vol 15, pg 69, 1999). Int J Plast 15(7):781–781
71. Patoor E, Eberhardt A, Berveiller M (1996) Micromechanical modelling of superelasticity in shape memory alloys. Le J de Physique IV 6(C1):C1-277-C1-292
72. Patoor E, El Amrani M, Eberhardt A, Berveiller M (1995) Determination of the origin for the dissymmetry observed between tensile and compression tests on shape memory alloys. Le J de Physique IV 5(C2):C2-495-C2-500
73. Farkas D, Roqueta D, Vilette A, Ternes K (1996) Atomistic simulations in ternary Ni-Ti-Al alloys. Model Simul Mater Sci Eng 4(4):359
74. Lai WS, Liu BX (2000) Lattice stability of some Ni-Ti alloy phases versus their chemical composition and disordering. J Phys Condens Matter 12(5):L53
75. Lai WS, Zhang Q, Liu BX, Ma E (2000) Structural stability and amorphization transition in the Ni–Ti system studied by molecular dynamics simulation with an n-body potential. J Phys Soc Jpn 69(9):2923–2937
76. Tirry W, Schryvers D (2005) Quantitative determination of strain fields around Ni_4Ti_3 precipitates in NiTi. Acta Mater 53(4):1041–1049
77. Bataillard L, Bidaux J-E, Gotthardt R (1998) Interaction between microstructure and multiple-step transformation in binary NiTi alloys using in-situ transmission electron microscopy observations. Philos Mag A 78(2):327–344